Temperature Rise under Two-Photon Optogenetic Brain Stimulation

Alexis Picot, Soledad Dominguez, Chang Liu, I-Wen Chen, Dimitrii Tanese, Emiliano Ronzitti, Pascal Berto, Eirini Papagiakoumou, Dan Oron, Gilles Tessier, et al.

Article

Cell Reports

Temperature Rise under Two-Photon Optogenetic Brain Stimulation

Graphical Abstract

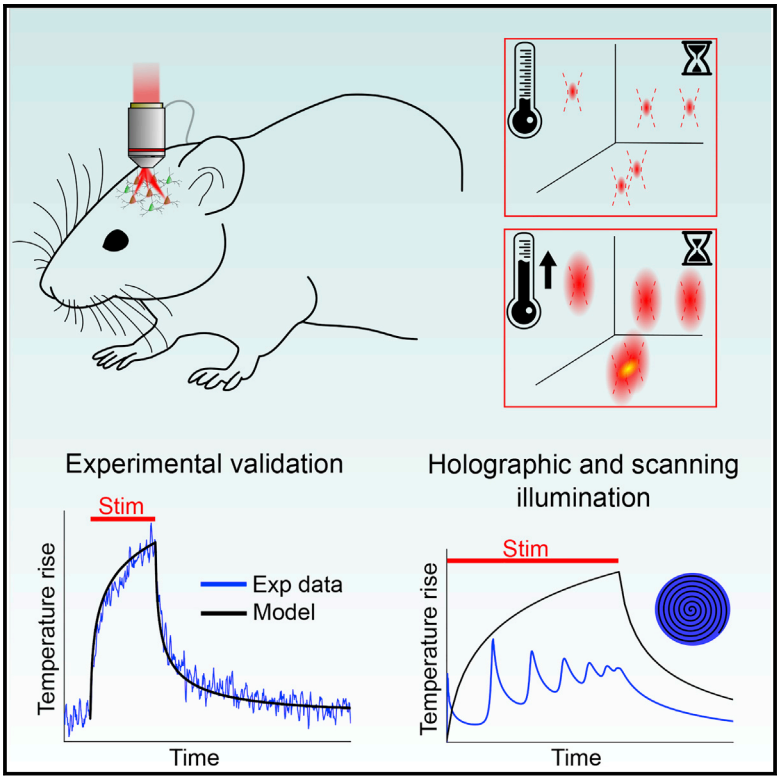

Authors

Alexis Picot, Soledad Dominguez, Chang Liu, ..., Gilles Tessier, Benoît C. Forget, Valentina Emiliani

Correspondence

valentina.emiliani@parisdescartes.fr

In Brief

Picot et al. model light and heat diffusion under the typical illumination conditions used for single- and multi-target two-photon optogenetics and compare the heat distribution under parallel and spiral scanning illumination. They experimentally validate the model using the temperature-dependent fluorescence of erbium-ytterbium co-doped glass particles.

Highlights

- *In vivo* multi-target 2P optogenetics might induce local sample heating
- A model is developed to predict and minimize sample heating
- The model can predict temperature rise under scanning and holographic illumination
- The model is validated using erbium-ytterbium co-doped glass particles

Picot et al., 2018, Cell Reports *24*, 1243–1253
July 31, 2018
https://doi.org/10.1016/j.celrep.2018.06.119

CellPress

Cell Reports
Article

Temperature Rise under Two-Photon Optogenetic Brain Stimulation

Alexis Picot,[1] Soledad Dominguez,[1] Chang Liu,[2,3] I-Wen Chen,[1] Dimitrii Tanese,[1] Emiliano Ronzitti,[1,3] Pascal Berto,[2] Eirini Papagiakoumou,[1,4] Dan Oron,[5] Gilles Tessier,[2,3] Benoît C. Forget,[1] and Valentina Emiliani[1,6,*]
[1]Wavefront-Engineering Microscopy Group, Neurophotonics Laboratory, UMR 8250 CNRS, University Paris Descartes, 45 rue des Saints-Pères, 75006 Paris, France
[2]Holographic Microscopy Group, Neurophotonics Laboratory, UMR 8250 CNRS, University Paris Descartes, 45 rue des Saints-Pères, 75006 Paris, France
[3]Sorbonne Université, CNRS, INSERM, Institut de la Vision, 17 Rue Moreau, 75011 Paris, France
[4]Institut National de la Santé et de la Recherche Médicale (Inserm), Paris, France
[5]Department of Physics of Complex Systems, Weizmann Institute of Science, Rehovot 76100, Israel
[6]Lead Contact
*Correspondence: valentina.emiliani@parisdescartes.fr
https://doi.org/10.1016/j.celrep.2018.06.119

SUMMARY

In recent decades, optogenetics has been transforming neuroscience research, enabling neuroscientists to drive and read neural circuits. The recent development in illumination approaches combined with two-photon (2P) excitation, either sequential or parallel, has opened the route for brain circuit manipulation with single-cell resolution and millisecond temporal precision. Yet, the high excitation power required for multi-target photostimulation, especially under 2P illumination, raises questions about the induced local heating inside samples. Here, we present and experimentally validate a theoretical model that makes it possible to simulate 3D light propagation and heat diffusion in optically scattering samples at high spatial and temporal resolution under the illumination configurations most commonly used to perform 2P optogenetics: single- and multi-spot holographic illumination and spiral laser scanning. By investigating the effects of photostimulation repetition rate, spot spacing, and illumination dependence of heat diffusion, we found conditions that make it possible to design a multi-target 2P optogenetics experiment with minimal sample heating.

INTRODUCTION

Over the past 15 years, optogenetics has become a unique and powerful tool for the investigation of brain circuits, with the capability of controlling neuronal firing and inhibition with millisecond precision and cell specificity (Emiliani et al., 2015).

Wide-field single-photon (1P) illumination is the most commonly used method to activate optogenetic actuators (Boyden et al., 2005; Nagel et al., 2005). Combined with strategies that restrict opsin expression in specific neuronal sub-populations (Beltramo et al., 2013; Cardin et al., 2009; Kuhlman and Huang, 2008) and/or optical fibers (Aravanis et al., 2007; Penzo et al., 2015; Wu et al., 2014) to reach deep brain regions, 1P wide-field illumination has been widely applied in neuroscience research, for example, inducing synaptic plasticity (Zhang and Oertner, 2007), mapping brain circuitry (Adesnik et al., 2012), and modulating behaviors (Adamantidis et al., 2007; Huber et al., 2008; Kitamura et al., 2017). Recently, additional strategies for 1P patterned illumination have made it possible to further increase photostimulation precision by restricting the illumination on specific brain layers (Pisanello et al., 2014) or cellular and subcellular structures (Guo et al., 2009; Petreanu et al., 2009; Szabo et al., 2014; Wyart et al., 2009). Yet the main constraint of 1P-based illumination approaches remains the limited spatial resolution and penetration depth: wide-field illumination makes it impossible to target an individual cell within a dense neuronal ensemble, while 1P patterned approaches have reached only shallow depths (Szabo et al., 2014).

This has spurred the development of more sophisticated light-delivering methods using two-photon (2P) excitation. These can be divided into two main categories: scanning approaches (Packer et al., 2012, 2015; Prakash et al., 2012; Rickgauer and Tank, 2009; Yang et al., 2018), in which cell photocurrent builds up thanks to the sequential photostimulation of channels or pumps expressed at the target membrane, and parallel approaches (low numerical aperture Gaussian beam, generalized phase contrast, computer-generated holography [CGH], temporal focusing), in which this is achieved by simultaneous illumination of the entire target (Bègue et al., 2013; Chaigneau et al., 2016; dal Maschio et al., 2017; Papagiakoumou et al., 2010; Rickgauer et al., 2014; Ronzitti et al., 2017). The combination of these approaches with *ad hoc* engineered control tools has enabled in-depth optical control of neuronal firing with millisecond temporal precision and cellular resolution (Ronzitti et al., 2017). Very recently, 2P illumination methods have been extended to the generation of three-dimensional (3D) illumination patterns. This has been achieved by spiral scanning multiplexed holographic foci (Packer et al., 2015; Yang et al., 2018) or by simultaneous shining of multiple spatiotemporally focused spots (Accanto et al., 2017; Hernandez et al., 2016; Pegard et al., 2017; Sun et al., 2018). These approaches combined with the use of

high-energy fiber lasers (Chaigneau et al., 2016; Ronzitti et al., 2017; Yang et al., 2018) and eventually highly sensitive opsins make it theoretically possible to simultaneously target hundreds of cells within cubic millimeter-size illumination volumes (i.e., comparable with what is achievable with single-fiber visible light illumination), preserving at the same time the single-cell resolution of 2P illumination. Yet setting the real limitations for multi-target 2P illumination requires considering possible sources of photodamage. These include both linear effects, such as thermal damage related to the linear absorption of light, and nonlinear, multiphoton absorption processes, inducing photochemical, ablation damage or optical breakdown (Hopt and Neher, 2001; Koester et al., 1999; Vogel et al., 2005) arising at peak fluences of about 0.1 J/cm^2 for Chinese hamster ovarian cells (König et al., 1999), 0.5–2 J/cm^2 in water (Linz et al., 2016; Noack and Vogel, 1999; Vogel et al., 2005), and 1.5–2.2 J/cm^2 for porcine corneal stroma (Olivié et al., 2008).

Because of the short dwell time and small illumination volume used in conventional multi-photon imaging, heating through linear absorption can be considered a negligible source of photodamage (Débarre et al., 2014; Kobat et al., 2009; Koester et al., 1999; Linz et al., 2016). Nevertheless, for repetitive scanning of large areas, this can become of increasing importance (Hopt and Neher, 2001; Podgorski and Ranganathan, 2016). Unlike 2P imaging, parallel optogenetic neuronal activation uses long (milliseconds to seconds) exposure time and/or large illumination area (or amount of targets), so thermal phenomena require a careful evaluation (Boulnois, 1986). Many neural functions can be altered when there is a change of temperature (Aronov and Fee, 2012; Christie et al., 2013; Elwassif et al., 2006; Kalmbach and Waters, 2012; Wang et al., 2014). Even small temperature changes can cause modulations of the action potential (AP) shape (Hodgkin and Katz, 1949), firing rate of neurons (Reig et al., 2010; Stujenske et al., 2015), channel conductance (Shibasaki et al., 2007; Wells et al., 2007), or fluctuation of the synaptic responses (Andersen and Moser, 1995; Thompson et al., 1985). Cell death after denaturation of proteins can also be expected after a temperature increase of 6–8 K above the physiological resting temperature (Deng et al., 2014; Thomsen, 1991). Notably, thermal damage thresholds also depend on brain area and specific tissue properties (Kiyatkin, 2007; Sharma and Hoopes, 2003).

Temperature rise under the typical illumination conditions for 1P optogenetics (i.e., wide-field illumination through optical fibers and long, 0.5–60 s exposure time) has been investigated both theoretically, using Monte Carlo with finite-difference time-domain schemes (Stujenske et al., 2015) or the finite-element method (Shin et al., 2016), and experimentally using thermocouples (Shin et al., 2016; Stujenske et al., 2015), quantum dots (Podgorski and Ranganathan, 2016), or infrared (IR) cameras (Arias-Gil et al., 2016).

Recently, Podgorski and his colleagues have modeled and measured heating under 20–180 s 2P repeated scanning illumination of a volume measuring 1 mm^2 in surface and 250 μm in depth (Podgorski and Ranganathan, 2016).

Despite these first investigations, a careful evaluation of brain heating under the different illumination conditions (parallel and scanning) used for 2P optogenetics is still missing.

In this paper, we present a theoretical model to describe light propagation and heat diffusion with millisecond precision and micrometer resolution under typical 2P excitation conditions that enable *in vivo* optogenetic control of neuronal firing. The model combines a random phase mask approach to account for 3D light scattering within tissue and Fourier's heat diffusion equation solved through Green's function formalism to evaluate the corresponding spatial and temporal heat diffusion during and after 2P photostimulation. We validated the model by comparing simulated and measured laser-induced temperature changes in a water/agar gel using the temperature dependent fluorescence emission of erbium-ytterbium (Er/Yb) co-doped glass particles. We then use the model to predict the temporal and spatial heat distribution in scattering media under different illumination conditions, including single- and multi-spot holographic illumination and spiral scanning. We analyze the 3D spatial and temporal evolution of temperature rise as a function of the stimulation frequency, laser repetition rate, and illumination duration.

The model is extendable to other illumination configurations, brain structures, and biological preparations with different scattering properties and is a unique and powerful tool to design the optimal illumination conditions for 2P optogenetics brain circuit control. The model has been implemented in a MATLAB (The MathWorks) package for use by other users to predict heat diffusion under their own 2P optogenetics experimental conditions.

RESULTS

Modeling Heat Diffusion

Heating during photostimulation (or any experimental procedure involving shining light on or in an object) results from the thermalization of the energy from the light source absorbed by the tissue.

To model heat diffusion, we considered brain tissue as a uniform and isotropic medium initially at temperature T_0, characterized by a thermal diffusion constant (or diffusivity) D, a specific heat C,and density ρ (see Table S1). The spatiotemporal distribution of the temperature rise $T(\vec{r},t)$, where $\vec{r}$ is the spatial coordinate in three dimensions and t is time, is obtained from Fourier's heat diffusion equation (Fourier, 1822):

$$\frac{\partial T(\vec{r},t)}{\partial t} = D\nabla^2 T(\vec{r},t) + \frac{q(\vec{r},t)}{\rho C}, \quad (1)$$

where $q(\vec{r},t) = \phi(\vec{r},t)\mu_a$ is the heat source term corresponding to the deposited energy flux per unit of volume from the absorption of laser power, $\phi(\vec{r},t)$ is the irradiance, and μ_a is the absorption coefficient of the medium. In the 950–1,030 wavelength range, water is the main source of absorption, while the contribution from hemoglobin is almost negligible. Therefore for all simulations (*in vitro* and *in vivo*), we used for μ_a the *ex vivo* value given in Yaroslavsky et al. (2002), which in this wavelength regime is very close to the *in vivo* situation (Johansson, 2010).

In living tissue, it is common to use the so-called Pennes bio heat equation (Pennes, 1948), which would add to the previous equation a source related to metabolic process, q_m , and a

sink (cooling) term related to blood perfusion, q_p , within the tissue:

$$\frac{\partial T(\vec{r},t)}{\partial t} = D\nabla^2 T(\vec{r},t) + \frac{q(\vec{r},t)}{\rho C} + \frac{q_m - q_p}{\rho C}. \quad (2)$$

The sink term is a function of the thermal properties of blood (ρ_b, C_b), blood flow w_b, and temperature T_b and is expressed as $q_p = \rho_b C_b w_b((T_0 + T(\vec{r},t)) - T_b)$. In physiological conditions q_m and q_p should be equal, maintaining tissue temperature constant.

If we take the characteristic values for ρ_b, C_b, and w_b (Elwassif et al., 2006; Stujenske et al., 2015) and we consider a tissue temperature rise of 1 K, we obtain for the sum of the source and sink term, $\frac{q_m - q_p}{\rho C}$, a value of roughly -9.2×10^{-3} K/s^{-1}. By taking for $q(\vec{r},t)$ under our experimental conditions a value of $\sim 6 \times 10^{-6}$ mW/μm^3 (with $\phi(\vec{r},t) \sim 0.1$ mW/μm^2 and $\mu_a = 6 \times 10^{-5}$ μm^{-1}), we obtain for $\frac{q(\vec{r},t)}{\rho C}$ a value of roughly 1.7×10^3 K/s^{-1}, with ρ and C taken from Blumm and Lindemann (2003) and Yizhar et al. (2011).

In agreement with previous findings (Elwassif et al., 2006; Stujenske et al., 2015), we can consider that under the experimental conditions considered in this paper, the main cooling mechanism is through diffusion. We therefore neglected the $\frac{q_m - q_p}{\rho C}$ term and used the Fourier's heat diffusion, Equation 1.

To solve Equation 1, we used Green's function formalism (Carslaw and Jaeger, 1947). Green's function $G(\vec{r},t)$ is the solution to an instantaneous point source of heat, and $T(\vec{r},t)$ is given by the convolution (over space and time) of this Green's function and the source term $q(\vec{r},t)$. For an infinite media (see STAR Methods), Green's function is readily obtained in analytical form for one-dimensional (1D) diffusion,

$$\frac{1}{\sqrt{4\pi Dt}} exp\left(-\frac{x^2}{4Dt}\right), \quad (3)$$

or 3D diffusion,

$$\frac{1}{(4\pi Dt)^{3/2}} exp\left(-\frac{r^2}{4Dt}\right), \quad (4)$$

where $r^2 = x^2 + y^2 + z^2$.

As Green's function for the diffusion equation is a Gaussian distribution, it is common, as seen for example in Bird et al. (1976), to define a diffusion length (here a thermal diffusion length) as the SD of this Gaussian distribution: $l_{th} = \sqrt{2nDt}$, where $n = 1, 2, 3$ is the dimensionality of the medium in which the diffusion process occurs.

Convolution of Green's function and the source term must then be carried out over space and time. In order to facilitate this convolution, we expressed the source term as a separable function of space and time, meaning as the product of the function describing independently the spatial and temporal distributions: $q(\vec{r},t) = \phi(\vec{r},t)\mu_a = \Gamma(\vec{r})\Pi(t)\mu_a$. Spatial distribution $\Gamma(\vec{r})$ and time dependence $\Pi(t)$ of the source term can therefore be treated separately. Further details describing the modeling of the light source propagation, the scattering, the time dependence of source term, and the trajectory of the laser beam can be found in the STAR Methods.

Experimental Validation of the Model

We tested the accuracy of our model by comparing the theoretical prediction with the measured temperature rise induced by a holographic spot focalized on a water/agar gel by embedding a micrometric Er/Yb co-doped glass particle in the gel (Figures S1A and S1B) and recording the luminescence spectral changes on the particle by the laser-induced heating (see STAR Methods).

We started by comparing simulations, with water coefficient of absorption taken from Kedenburg et al. (2012), with experiments in the case of a 500 ms stimulation at 1,030 nm wavelength (laser pulse width $\sim$ 250 fs, repetition rate 10 MHz) focalized to a 15-μm-diameter holographic spot placed 30 μm away from the particle, and we found that our prediction perfectly reproduced both the magnitude and the temporal evolution of the temperature rise (Figure 1A, left). To validate the ability of the model to account for the spatial heat distribution, we compared the predicted and experimental values of the temperature rise reaching 500 ms after optical excitation, while laterally moving the illumination spot with respect to the particle (Figure 1A, right). Finally, we exploit the capability of the model to predict the fast temperature changes and temperature accumulation produced by 2 or 10 Hz stimulation trains (Figure 1B) of 50 ms illumination pulses.

Single-Spot Holographic Photostimulation

Here, we use the model to predict the temperature changes produced under exemplary illumination condition for 2P optogenetics using parallel (holographic) illumination (Chen et al., 2017). Figure 2A (left) shows the simulated temperature change produced by a single holographic spot after propagation through 150 μm of brain tissue (see STAR Methods and Figure S2A) using exemplary conditions for *in vivo* AP generation (Figure 2A, right; see STAR Methods) using the opsin CoChR. At the end of the 3 ms illumination time, the model predicts a mean temperature increase of the cell of 0.3 K followed by a rapid temperature decay (reaching 0.05 K after 10 ms). It should be noted that although the temperature increase has a linear dependence with the excitation power, it is not linear with exposure time when diffusion is taken into account. This sublinear dependence can be expressed in terms of the complementary error function, and for the typical conditions considered in this paper, increasing the exposure time of a factor of 10 raises the temperature only by a factor of roughly 2 (Figure S3B). Although at the onset of heat diffusion, the temperature distribution reproduces the speckled intensity distribution typical of CGH, these fluctuations are washed out as soon as the thermal diffusion length ($l_{th} = \sqrt{6Dt}$) equals the speckle size ($l_{th} \approx \lambda = 1,03\ \mu m$; i.e., for $t \geq 1\ \mu s$) (Figure S3A). We then simulated the effect on thermal response when the same stimulation (illumination time = 3 ms) was repeated at a rate of 10 or 40 Hz (Figure 2B, left) to produce AP trains (Figure 2B, right). As

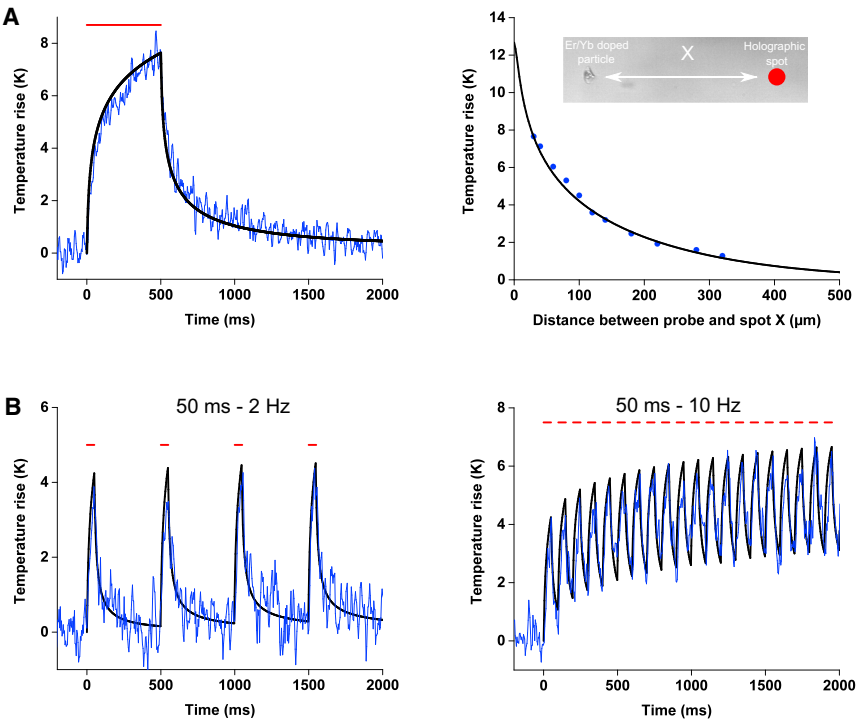

Figure 1. Validation of the Thermal Simulations through Experimental Luminescence Recordings

(A) Left: simulation (black trace) and experimental measurement (blue trace) of the temperature rise induced by a 15-μm-diameter holographic spot (500 mW average power, 500 ms illumination time, 1,030 nm excitation wavelength, 10 MHz repetition rate, ~250 fs laser pulse duration) placed at 30 μm from an Er/Yb co-doped particle placed in water/agar gel (mass fraction of agar 0.005) at a depth of 150 μm. Right: simulation and experimental measurement of the peak temperature rise as a function of the distance X between the particle and the holographic spot using the same illumination conditions as in (A, left). Scale bar, 10 μm.

(B) Simulation (black trace) and experimental measurement (blue trace) of the temperature rise induced by a 2 Hz (left) and 10 Hz (right) train of 50 ms illumination pulses, using the same illumination conditions as in (A) with the spot placed at 30 μm from the particle.

we can observe, under 10 Hz stimulation, the heat dissipation after each photostimulation pulse is fast enough to bring the cell back to the equilibrium temperature before the arrival of the next photostimulation pulse. Increasing the stimulation repetition rate generates a heat accumulation after each photostimulation pulse. However, even at a rate of 100 Hz, after five pulses, the accumulated temperature rise does not exceed a few tenths of a degree (Figure 2C); of course this accumulation becomes more relevant for longer illumination times (Figure S3B).

Multi-spot Holographic Photostimulation

Here, we consider the temperature rise induced by multiple spots distributed in a volume. In this case, it is important to consider for each plane the different attenuation of light due to scattering. To this end, the light distribution is obtained by using a holographic phase mask that compensates for the depth-dependent light losses and produces, at each focal depth, holographic spots of equal excitation density. Using a 3D fluorescence stack as a guide (Figure 3A) for placing the spots in three dimensions, we generated 100 holographic spots within a 300 × 300 × 300 μm^3 volume (excitation power density at each spot ~ 0.07 $mW/\mu m^2$) and used our model to predict the corresponding 3D spatiotemporal evolution of the temperature rise (Figure 3B; Video S1). At the end of the 3 ms stimulation, we found a mean temperature rise, averaged over the 100 spots, of ~1 K (Figure 3C). Because of the high density of spots, the value of the temperature rise at each spot obviously depends on the number and locations of the neighboring spots. For example, at spots generated in the deeper layers and surrounded by several neighboring spots, the local temperature rise can reach up to 1.85 K (Figure 3C), while for spots placed at an average distance greater than the thermal diffusion length ($l_{th} = \sqrt{6Dt}$ ~ 50 μm) from their nearest neighbor, the temperature rise remains around 0.3 K (i.e., comparable with the case of the isolated spot reported in Figure 2A).

Simulation of Heating Effect for Different Illumination Conditions

Here, we show how our model can simulate the spatiotemporal temperature distribution generated under spiral scanning illumination and compare the corresponding heat distribution with the one obtained using holographic illumination.

To quantitatively compare the two approaches, we first determined for each of these two approaches the power conditions that allow *in vitro* AP generation with comparable latencies. To this end, we used an optical system able to perform sequentially holographic and spiral scanning photostimulation on the same cell (see STAR Methods). We found that for both short (3 ms) and long (40 ms) illumination times, the average power necessary to evoke an AP using holographic illumination was roughly twice larger than with the scanning approach (37.5 and 16 mW on average [n = 3] for 3 ms illumination, 5.8 and 2.5 mW on average [n = 4] for 40 ms illumination; Figure 4A). Of note, the larger spot in holographic excitation enables the use of a power density roughly 150 times smaller (0.2 versus 31 $mW/\mu m^2$ for 3 ms illumination, 0.03 versus 5 $mW/\mu m^2$ for 40 ms illumination). These results confirm what has been recently achieved *in vivo* using the C1V1 opsin and a laser source tuned to 1 MHz (average power for spiral scanning about 1.8 lower than the one used for a 12-μm-diameter holographic spot) (Yang et al., 2018).

These power values were used to simulate the spatiotemporal distribution of the temperature rise using holographic

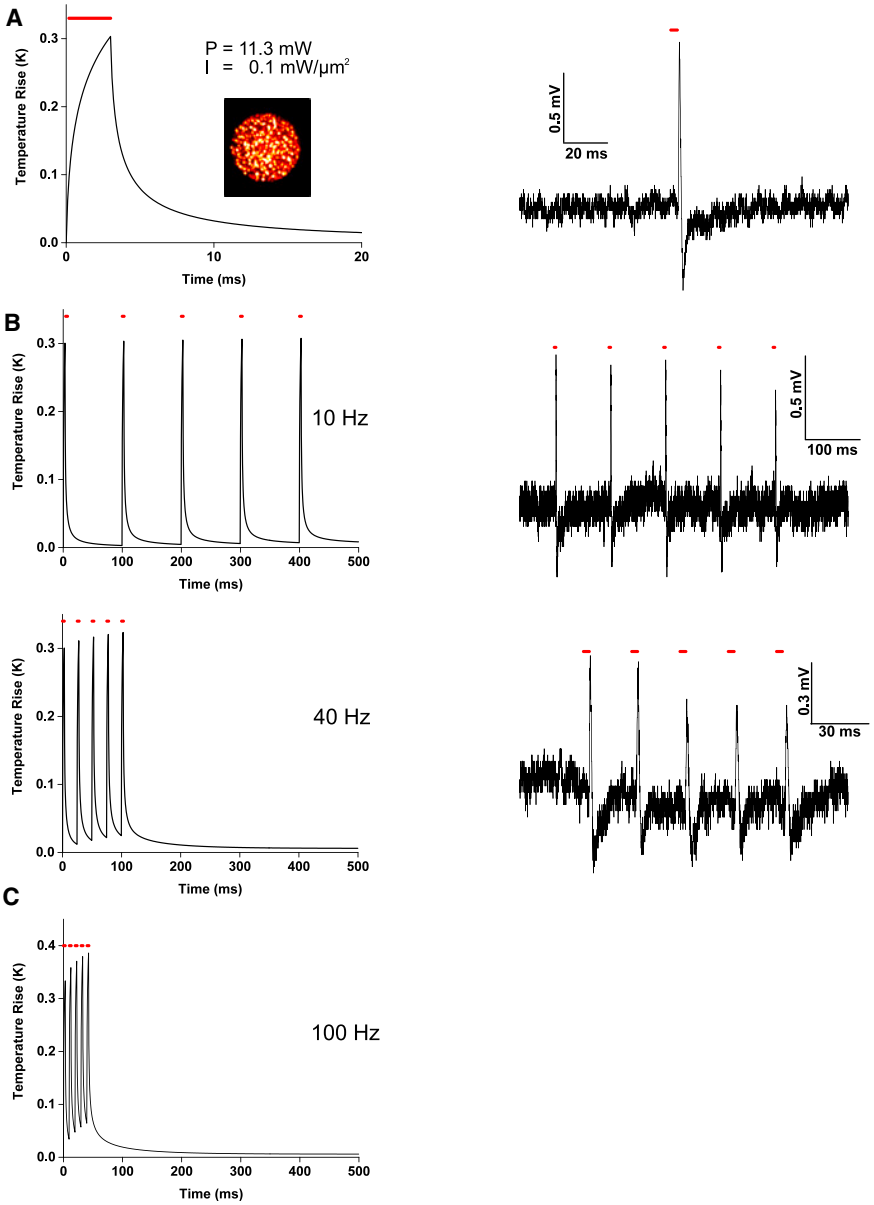

Figure 2. Simulated Temperature Rise Produced by a Holographic Spot Using the Photostimulation Conditions Necessary to Evoke *In Vivo* Action Potential

(A) Left: temperature rise, averaged on the spot surface, produced by a 12-μm-diameter holographic spot at a depth of 150 μm during 3 ms illumination, 1,030 nm excitation wavelength, 500 kHz repetition rate, 250 fs laser pulse duration, 11.3 mW excitation average power at the objective focal plane corresponding to ~0.07 mW/ μm^2 at a depth of 150 μm (and to 0.1 mW/ μm^2 excitation power density in the absence of scattering). Right: *in vivo* voltage recordings in cell-attached configuration from a CoChR-expressing cortical neuron upon photostimulation with the parameters used for the simulation in (A, left) evoking an action potential.

(B) Left: temperature rise, averaged on the spot surface, produced by a 12-μm-diameter holographic spot during a train of five illuminations of 3 ms at 10 or 40 Hz using the conditions described in (A). Right: experimental voltage recordings in cell-attached configuration *in vivo* from a CoChR-expressing cortical neuron upon photostimulation using the same parameters as in the left panel. Action potentials were induced upon each photostimulation with trains of 3 ms light pulse (red mark).

(C) Temperature rise, averaged on the spot surface, produced by a 12-μm-diameter holographic spot during a train of five illuminations pulses of 3 ms at 100 Hz.

(Figure 4B) and spiral scanning illuminations (Figure 4C) and two illumination durations (3 and 40 ms). The maximum mean temperature is reached, as expected, at the end of the illumination time. After 3 ms of illumination (Figure 4B, left; Figure 4C, left; Video S3), it equals ~1.1 K for CGH and ~0.5 K for scanning. In the latter case, the accumulation of heat during the scan leads to a localized temperature peak of ~1.1 K (about 2 times higher than the average value) when the laser reaches the center of the spiral. Also, the model makes it possible to predict temperature oscillations at the edge of the cell during the seven scanning loops. Using longer illumination times (40 ms) makes it possible to decrease the excitation power, although it also increases the AP latency; in this case the mean temperature stays below ~0.25 and ~0.12 K for CGH and scanning, respectively, with a local maximum of ~0.2 K at the center of the cell in the case of spiral scanning (Figure 4B, right; Figure 4C, right).

DISCUSSION

In this study, we provide a method able to measure and predict the temperature changes induced by 2P illumination with micrometer precision and millisecond temporal resolution, under the typical condition used for *in vitro* and *in vivo* 2P optogenetics stimulation.

Combining a random phase mask approach with the Fourier's heat diffusion equation to account for 3D light scattering and heat diffusion within tissue, the model makes it possible to follow the 3D spatiotemporal evolution of temperature rise both under single and multi-target activation.

Previous approaches such as Monte Carlo simulations with finite-difference time-domain (FDTD) methods (Stujenske et al., 2015) or empirical fitting of experimental results (Arias-Gil et al., 2016; Podgorski and Ranganathan, 2016) did not reach micrometer and millisecond resolution. Indeed, to simulate the propagation of tightly focused beams would require introducing diffraction in the Monte Carlo code, which is intrinsically difficult

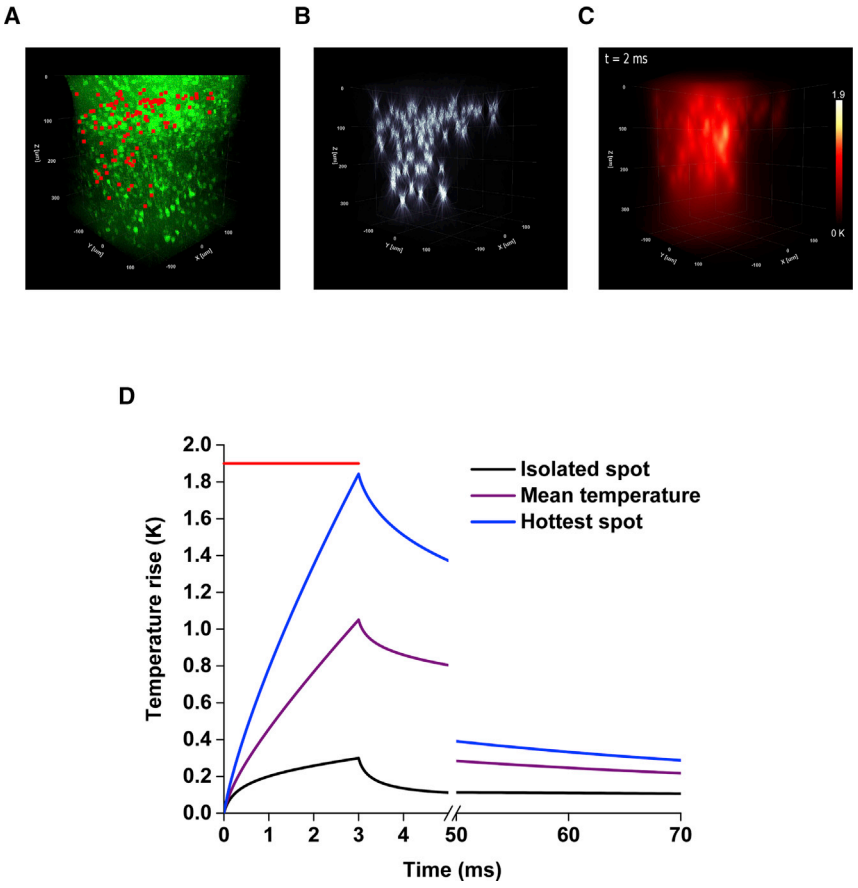

Figure 3. Simulated Temperature Rise Produced by Multiple Holographic Spots at the Photostimulation Conditions Necessary to Evoke *In Vivo* Action Potential

(A) Three-dimensional view of an *in vivo* two-photon fluorescence stack of the layer 2/3 of mouse visual cortex labeled with GFP with in red locations of the 100 holographic spots.

(B) Three-dimensional spatial distribution of irradiance produced by 100 holographic spots (12 μm diameter, 0.1 mW/μm^2, 1,030 nm) placed in a 300 × 300 × 300 μm^3 volume, with scattering compensated for *in vivo* conditions.

(C) Three-dimensional spatial distribution of the temperature rise produced by 100 holographic spots (12 μm diameter, 0.1 mW/μm^2, 1,030 nm) placed in a 300 × 300 × 300 μm^3 volume, after 2 ms of illumination.

(D) Examples of traces of the temporal evolution of the temperature rise, averaged on the spot surface, produced by 3 ms of illumination with the spots distribution described in (B) and the illumination conditions described in Figure 2 for an isolated spot (black curve) and a spot chosen in the area with high density of spots (blue curve). The purple curve represents the meant temperature rise averaged over the 100 spots.

(Brandes et al., 2014). Furthermore, for holographic beams, a Monte Carlo approach would need to simulate the propagation of the electromagnetic field, which is much more complex than the traditional Monte Carlo schemes on the basis of the propagation of the intensity. On the other hand, FDTD methods require extra care in setting the spatial and time discretization steps in order to assure stability and avoid spurious oscillations in the numerical solution. For a Crank-Nicolson scheme (Crank and Nicolson, 1947), this required satisfying the condition $\frac{D\Delta t}{\Delta x^2} < \frac{1}{2}$ with D the thermal diffusivity, which bounds the spatial and the temporal resolution. For example, following the time interval of 3 ms with a micrometer resolution of $\Delta x = 0.5\ \mu m$ would imply setting $\Delta t \approx 1\ \mu s$ and therefore using 3,000 iterations. Other numerical schemes can be used to solve the heat diffusion equation, but in all cases, they are iterative processes and therefore are by themselves time consuming, particularly if high accuracy is needed. Empirical fitting of temperature measurements is intrinsically limited to the experimental spatial and temporal resolution, which so far were significantly above the micrometer and millisecond scale.

On the other hand, using the analytical expression of the Green's function gives us the possibility to simulate the spatial distribution of temperature with micrometer spatial precision and submillisecond temporal resolution and discuss the results from the simulation on the basis of a physical parameter that is the thermal diffusion length, l_{th}.

So far, experimental methods to evaluate light induced heating during optogenetics experiments have used thermocouples, with millimeter-long tips and diameters ranging between 220 and 500 μm, which translates into a millimeter-range sensitive region (Podgorski and Ranganathan, 2016; Shin et al., 2016; Stujenske et al., 2015), or a thermal camera allowing a spatial resolution of ∼50 μm (Arias-Gil et al., 2016). These probes were well adapted to measure temperature rises averaged on large area but lack the necessary precision to predict the spatial heat distribution induced by 2P patterned light at micrometer scale. The use of quantum dot thermometry could reduce the spatial resolution down to the micrometer scale but required long (typically ∼1 s) integration time (Podgorski and Ranganathan, 2016).

Here, we quantify (at high spatiotemporal resolution) the temperature response induced by 2P excitation by using rare-earth doped glass particles. Such particles have the property of emitting a strong temperature-dependent luminescent signal (Aigouy et al., 2005; Saïdi et al., 2009). By probing a single ∼10 μm Er/Yb co-doped particle, we manage to significantly increase the photon budget to reach a thermal sensitivity below 0.2 K, a temporal resolution of 4 ms, while reducing the size of the probed region down to a spatial scale comparable with the neuron cell body. To efficiently sample the temporal evolution of heating, we used here illumination pulses > 50 ms. More efficient detection schemes will increase sensitivity, enabling higher sampling rates and thus the use of shorter illumination pulses. However, the Er/Yb co-doped particle lifetime will limit the resolution to ∼0.5 ms (Wang et al., 2016).

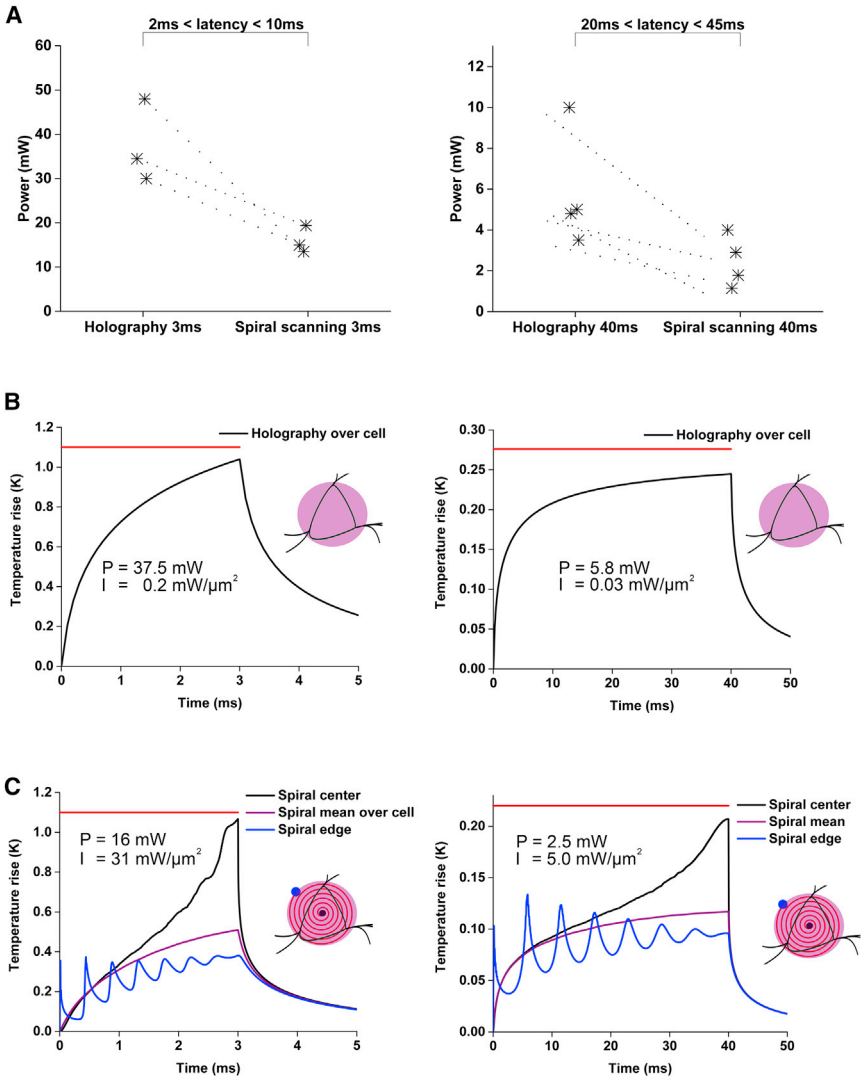

Figure 4. Simulated Temperature Rise and Experimental Electrophysiological Recordings with CGH and Scanning Illumination Techniques

(A) Left: excitation average power needed to generate in CoChR-expressing neuronal brain slices a single AP with a latency between 2 and 10 ms using a 15-μm-diameter holographic spot illumination for 3 ms, or spiral scanning (seven revolutions moving from the edge to the center, 15 μm diameter) for the same duration, 3 ms (laser excitation 1,030 nm, 2 MHz repetition rate, ~300 fs laser pulse duration). Right: excitation power needed to generate in CoChR-expressing cell in acute brain slices a single AP with a latency between 20 and 45 ms using a holographic illumination for 40 ms, or spiral scanning (seven revolutions moving from the edge to the center, 15 μm diameter) for the same duration, 40 ms (laser excitation 1,030 nm, 2 MHz repetition rate, ~300 fs laser pulse duration).

(B) Left: temperature rise averaged on the spot surface, produced using the holographic illumination condition of the experiments of (A, left) and 37.5 mW excitation average power. Right: temperature rise averaged on the spot surface, produced using the holographic illumination condition of the experiments of (B, right) and 5.8 mW average power.

(C) Left: Temperature rise, using the spiral illumination condition of the experiments of (A, left) and 16 mW excitation average power. Right: temperature rise, produced using the spiral illumination conditions of the experiments of (B, right) and 2.5 mW average power. In blue, temperature rise at the beginning, on the edge. In black, the temperature rise at the center of the spiral. In red, the temperature rise averaged over a disc of 15 μm.

After experimental verification of the validity of the model, we have used this to evaluate the spatiotemporal heat distribution under the most commonly used configurations for 2P optogenetics control of neuronal firing: holographic and scanning illumination.

Holographic parallel illumination combined with amplified low-repetition rate lasers and sensitive opsins makes it possible to evoke AP and AP trains *in vivo* using low excitation density (<0.1 mW/μm^2) and short illumination time (<3 ms) (Chen et al., 2017). Using our model we have shown that these illumination conditions correspond to less than 0.35 K of mean temperature increase for single-cell activation (Figure 2).

In 2P CGH, the intensity distribution of the excitation patterns present spatial intensity fluctuations that could reach 50% around the mean value (Papagiakoumou et al., 2008), which could generate localized hotspots. However, we could show that this speckled distribution is preserved in the heating profile only for the first few microseconds, being quickly smoothed out by diffusion. Within this short time, the temperature rise even at the hottest spots will not exceed a few millikelvin, thus ruling out the risk that holographic speckles can induce local hotspots.

The generation of trains of pulses had no effect on the total temperature rise, for a stimulation frequency of 10 Hz and 3 ms illumination time (Figure 2B). For higher stimulation frequency, when the delay between pulses becomes comparable with the heating decay time, repetitive pulse stimulation will induce heating accumulation, but even for the case of 100 Hz stimulation, this will be less than 0.1 K (Figure 2C).

For prolonged (seconds to minutes) scanning illuminations of large area (square millimeters), the highest temperature change is deeper in the brain than at the focal plane (Podgorski and Ranganathan, 2016) (see STAR Methods), while for the spatially localized and short (milliseconds) illumination conditions used in 2P optogenetics, the highest temperature changes occurred within the spots (Figure 3B), suggesting that these are the positions where it is important to evaluate the maximum temperature rise. We have shown that the simultaneous illumination with 100 spots, placed in a 300 × 300 × 300 μm^3 volume, makes it possible to keep the temperature rise at the targets comparable

with the case of an isolated cell, provided that the spatial distance among the targets is kept larger than the 3D diffusion length (Figure S4; Video S2).

We have shown that our model can be applied to predict temperature rise both under parallel and spiral scanning optogenetic illuminations. In scanning approaches, the excitation light is focused on a small spot, and photocurrent builds up thanks to the sequential opening of channels. This enables using lower illumination power than the one used in holographic photostimulation, for which, on the contrary, current integration is achieved by simultaneous activation of all channels. The smaller spot size used in spiral scanning also enables more efficient heat dissipation, so that overall spiral scanning leads to lower temperature rise. On the other hand, the concentration of light on a small spot leads to power densities 150 times higher than the one used in CGH and closer to nonlinear photodamage thresholds so that, especially for short illumination times, care needs to be taken in limiting the number of successive scans (Hopt and Neher, 2001).

These results also indicate that the optimal laser repetition rate for 2P optogenetics depends on the adopted illumination methods: the extremely low excitation power density adopted for parallel illumination approaches (Figure 4B: peak fluence ≈ 10.7 and 1.7 mJ/cm^2, respectively, for 3 and 40 ms illumination conditions; Figure 2: peak fluence ≈ 20 mJ/cm^2) makes it possible to neglect nonlinear damage effect and privileges using low (500 kHz to 2 MHz) repetition rate lasers to minimize heating through linear absorption. Scanning approaches require higher excitation power density (Figure 4C: peak fluence ≈ 1.6 and 0.25 J/cm^2, respectively, for 3 and 40 ms illumination conditions) but enable more efficient heat dissipation; therefore, for short illumination times, a higher repetition rate laser (Ji et al., 2008) should be preferred in order to minimize peak-power-sensitive damages.

Here, we used for both approaches the opsin CoChR, which has intermediate rise (~6 ms) and decay (~35 ms) times (Shemesh et al., 2017). For parallel approaches, similar excitation power density and illumination times can be reached independently on the opsin kinetics (Chaigneau et al., 2016; Chen et al., 2017; Ronzitti et al., 2017); therefore we can expect similar values of temperature rises. On the contrary, illumination conditions for spiral scanning are more sensitive to the opsin kinetics: combination with a slower opsin such as C1V1 makes it possible to lower the power (Yang et al., 2018) and therefore reduce the temperature rise even further, while combined with faster opsins as Chronos would require the use of higher powers to compensate for the fast channel off-time.

Our model is extendable to other brain regions or biological preparations differing in scattering properties, thus offering a unique and flexible tool for the design of complex optogenetics experiments with minimal sample heating. It will surely prove useful also to simulate the temperature distribution under different excitation configurations (including single- and three-photon excitation) and imaging geometries (e.g., light sheet microscopy, stimulated emission depletion microscopy, or Bessel beam illumination) or to optimize light distribution and illumination conditions for thermogenetic experiments (Bernstein et al., 2012; Ermakova et al., 2017; Hamada et al., 2008).

STAR★METHODS

Detailed methods are provided in the online version of this paper and include the following:

- KEY RESOURCES TABLE
- CONTACT FOR REAGENT AND RESOURCE SHARING
- EXPERIMENTAL MODEL AND SUBJECT DETAILS
  - Mice for *in vivo* experiments
  - Mice for in-vitro experiments
- METHOD DETAILS
  - Virus injection and surgical procedures – In-vivo
  - 2P-guided electrophysiology – in-vivo
  - Holographic photostimulation – in-vivo
  - Brain slices
  - Whole-cell recordings – in-vitro
  - 2P holographic and spiral scanning photostimulation – in-vitro
  - Modeling – Light source propagation and scattering
  - Modeling – Time dependence of source term
  - Modeling – Convolution with separable source term
  - Modeling – Moving laser spot
  - Modeling – The infinite media hypothesis
  - Thermal measurement
  - Thermal measurement – Calibration of the probe
- QUANTIFICATION AND STATISTICAL ANALYSIS
- DATA AND SOFTWARE AVAILABILITY

SUPPLEMENTAL INFORMATION

Supplemental Information includes four figures, one table, three videos, and one data file and can be found with this article online at https://doi.org/10.1016/j.celrep.2018.06.119.

ACKNOWLEDGMENTS

We acknowledge the SCM (Service Commun de Microscopie – Faculté des Sciences Fondamentales et Biomédicales – Paris) for providing the software Imaris (version 8.4; Bitplane; www.bitplane.com) and 3i for technical support in the implementation of spiral scanning. We thank Agence Nationale de la Recherche (grants ANR-14-CE13-0016 [Holohub] and ANR-15-CE19-0001-01 [3DHoloPAc]), the Human Frontiers Science Program (grant RGP0015/2016), Région Ile de France (Projet GeneTherm – C'Nano – DIM Nano-K 2016), Fondation Bettencourt Schueller (Prix Coups d'élan pour la recherché française), and the Getty Lab for financial support. I.-W.C. received funding from the European Union's Horizon 2020 research and innovation program under Marie Skłodowska-Curie grant agreement 747598. We thank Patrick Gredin and Michel Mortier, from Chimie Paris, who developed and fabricated the Er/Yb glass particles, and Aurelien Clavé, who contributed to the early development of the temperature measurement technique. We thank Deniz Dalkara for providing the GFP viral construct and Valeria Zampini for performing injections. Icons made by Freepik (www.flaticon.com) for graphical abstract and mouse design from Gwilz.

AUTHOR CONTRIBUTIONS

A.P. implemented the Python code into a MATLAB package and combined it with the random phase mask code and performed the simulations. S.D. performed *in vitro* electrophysiological experiments and analyzed the data. C.L. designed the agar phantoms and carried out the temperature measurements. I.-W.C. performed the *in vivo* electrophysiological experiments and performed virus injections. D.T. designed and built up the scanning-holography system and participated in the *in vitro* experiments and the temperature measurement.

E.R. and E.P. built up the *in vivo* holographic system and participated in the *in vivo* optogenetics experiments. P.B. and G.T. designed and developed the temperature measurement technique. D.O. wrote the code for the random phase mask approach. B.C.F. created the theory and developed a first Python code for heat diffusion simulation. V.E. wrote the paper with A.P. and B.C.F. and conceived and supervised the project.

DECLARATION OF INTERESTS

The authors declare no competing interests.

Received: August 9, 2017
Revised: March 26, 2018
Accepted: June 28, 2018
Published: July 31, 2018

REFERENCES

Accanto, N., Tanese, D., Ronzitti, E., Molinier, C., Newman, Z.L., Wyart, C., Ehud, I., Eirini, P., and Emiliani, V. (2017). Multiplexed temporally focused light shaping for high-resolution multi-cell targeting. bioRxiv, https://www.biorxiv.org/content/early/2017/11/08/216135.

Adamantidis, A.R., Zhang, F., Aravanis, A.M., Deisseroth, K., and de Lecea, L. (2007). Neural substrates of awakening probed with optogenetic control of hypocretin neurons. Nature *450*, 420–424.

Adesnik, H., Bruns, W., Taniguchi, H., Huang, Z.J., and Scanziani, M. (2012). A neural circuit for spatial summation in visual cortex. Nature *490*, 226–231.

Aigouy, L., Tessier, G., Mortier, M., and Charlot, B. (2005). Scanning thermal imaging of microelectronic circuits with a fluorescent nanoprobe. Appl. Phys. Lett. *87*, 1–3.

Andersen, P., and Moser, E.I. (1995). Brain temperature and hippocampal function. Hippocampus *5*, 491–498.

Aravanis, A.M., Wang, L.-P., Zhang, F., Meltzer, L.A., Mogri, M.Z., Schneider, M.B., and Deisseroth, K. (2007). An optical neural interface: in vivo control of rodent motor cortex with integrated fiberoptic and optogenetic technology. J. Neural Eng. *4*, S143–S156.

Arias-Gil, G., Ohl, F.W., Takagaki, K., and Lippert, M.T. (2016). Measurement, modeling, and prediction of temperature rise due to optogenetic brain stimulation. Neurophotonics *3*, 045007.

Aronov, D., and Fee, M.S. (2012). Natural changes in brain temperature underlie variations in song tempo during a mating behavior. PLoS ONE *7*, e47856.

Bègue, A., Papagiakoumou, E., Leshem, B., Conti, R., Enke, L., Oron, D., and Emiliani, V. (2013). Two-photon excitation in scattering media by spatiotemporally shaped beams and their application in optogenetic stimulation. Biomed. Opt. Express *4*, 2869–2879.

Beltramo, R., D'Urso, G., dal Maschio, M., Farisello, P., Bovetti, S., Clovis, Y., Lassi, G., Tucci, V., De Pietri Tonelli, D., and Fellin, T. (2013). Layer-specific excitatory circuits differentially control recurrent network dynamics in the neocortex. Nat. Neurosci. *16*, 227–234.

Bernstein, J.G., Garrity, P.A., and Boyden, E.S. (2012). Optogenetics and thermogenetics: technologies for controlling the activity of targeted cells within intact neural circuits. Curr. Opin. Neurobiol. *22*, 61–71.

Bird, R.B., Stewart, W.E., and Lightfoot, E.N. (1976). Transport Phenomena (New York: John Wiley).

Blumm, J., and Lindemann, A. (2003). Characterization of the thermophysical properties of molten polymers and liquids using the flash technique. High Temp. High Press. *35–36*, 627–632.

Boulnois, J.L. (1986). Photophysical processes in recent medical laser developments: a review. Lasers Med. Sci. *1*, 47–66.

Boyden, E.S., Zhang, F., Bamberg, E., Nagel, G., and Deisseroth, K. (2005). Millisecond-timescale, genetically targeted optical control of neural activity. Nat. Neurosci. *8*, 1263–1268.

Brandes, A.R., Elmaklizi, A., Akarçay, H.G., and Kienle, A. (2014). Modeling the tight focusing of beams in absorbing media with Monte Carlo simulations. J. Biomed. Opt. *19*, 115003.

Cardin, J.A., Carlén, M., Meletis, K., Knoblich, U., Zhang, F., Deisseroth, K., Tsai, L.-H., and Moore, C.I. (2009). Driving fast-spiking cells induces gamma rhythm and controls sensory responses. Nature *459*, 663–667.

Carslaw, H.S., and Jaeger, J.C. (1947). Conduction of Heat in Solids (Oxford Science Publications).

Chaigneau, E., Ronzitti, E., Gajowa, M.A., Soler-Llavina, G.J., Tanese, D., Brureau, A.Y.B., Papagiakoumou, E., Zeng, H., and Emiliani, V. (2016). Two-photon holographic stimulation of ReaChR. Front. Cell. Neurosci. *10*, 234.

Chen, I.-W., Ronzitti, E., Lee, B.R., Daigle, T.L., Zeng, H., Papagiakoumou, E., and Emiliani, V. (2017). Parallel holographic illumination enables sub-millisecond two-photon optogenetic activation in mouse visual cortex in vivo. bioRxiv, https://www.biorxiv.org/content/early/2018/01/21/250795.

Christie, I.N., Wells, J.A., Southern, P., Marina, N., Kasparov, S., Gourine, A.V., and Lythgoe, M.F. (2013). fMRI response to blue light delivery in the naïve brain: implications for combined optogenetic fMRI studies. Neuroimage *66*, 634–641.

Crank, J., and Nicolson, P. (1947). A practical method for numerical evaluation of solutions of partial differential equations of the heat-conduction type. Math. Proc. Camb. Philos. Soc. *43*, 50–67.

dal Maschio, M., Donovan, J.C., Helmbrecht, T.O., and Baier, H. (2017). Linking neurons to network function and behavior by two-photon holographic optogenetics and volumetric imaging. Neuron *94*, 774–789.e5.

Dantelle, G., Mortier, M., Vivien, D., and Patriarche, G. (2005). Nucleation efficiency of erbium and ytterbium fluorides in transparent oxyfluoride glass-ceramics. J. Mater. Res. *20*, 472–481.

Débarre, D., Olivier, N., Supatto, W., and Beaurepaire, E. (2014). Mitigating phototoxicity during multiphoton microscopy of live Drosophila embryos in the 1.0-1.2 μm wavelength range. PLoS ONE *9*, e104250.

Deng, W., Goldys, E.M., Farnham, M.M.J., and Pilowsky, P.M. (2014). Optogenetics, the intersection between physics and neuroscience: light stimulation of neurons in physiological conditions. Am. J. Physiol. Regul. Integr. Comp. Physiol. *307*, R1292–R1302.

Elwassif, M.M., Kong, Q., Vazquez, M., and Bikson, M. (2006). Bio-heat transfer model of deep brain stimulation-induced temperature changes. J. Neural Eng. *3*, 306–315.

Emiliani, V., Cohen, A.E., Deisseroth, K., and Häusser, M. (2015). All-optical interrogation of neural circuits. J. Neurosci. *35*, 13917–13926.

Ermakova, Y.G., Lanin, A.A., Fedotov, I.V., Roshchin, M., Kelmanson, I.V., Kulik, D., Bogdanova, Y.A., Shokhina, A.G., Bilan, D.S., Staroverov, D.B., et al. (2017). Thermogenetic neurostimulation with single-cell resolution. Nat. Commun. *8*, 15362.

Fourier, J. (1822). Fourier: Théorie Analytique de la Chaleur (Chez Firmin Didot, Père et Fils).

Goodman, J.W. (1996). Introduction to Fourier optics McGraw-Hill Series in Electrical and Computer Engineering. Quantum Semiclassical Opt. J. Eur. Opt. Soc. Part B *8*, 491.

Guo, Z.V., Hart, A.C., and Ramanathan, S. (2009). Optical interrogation of neural circuits in Caenorhabditis elegans. Nat. Methods *6*, 891–896.

Hamada, F.N., Rosenzweig, M., Kang, K., Pulver, S.R., Ghezzi, A., Jegla, T.J., and Garrity, P.A. (2008). An internal thermal sensor controlling temperature preference in Drosophila. Nature *454*, 217–220.

Hernandez, O., Papagiakoumou, E., Tanese, D., Fidelin, K., Wyart, C., and Emiliani, V. (2016). Three-dimensional spatiotemporal focusing of holographic patterns. Nat. Commun. *7*, 11928.

Hodgkin, A.L., and Katz, B. (1949). The effect of sodium ions on the electrical activity of giant axon of the squid. J. Physiol. *108*, 37–77.

Hopt, A., and Neher, E. (2001). Highly nonlinear photodamage in two-photon fluorescence microscopy. Biophys. J. *80*, 2029–2036.

Huber, D., Petreanu, L., Ghitani, N., Ranade, S., Hromádka, T., Mainen, Z., and Svoboda, K. (2008). Sparse optical microstimulation in barrel cortex drives learned behaviour in freely moving mice. Nature *451*, 61–64.

Ji, N., Magee, J.C., and Betzig, E. (2008). High-speed, low-photodamage nonlinear imaging using passive pulse splitters. Nat. Methods *5*, 197–202.

Johansson, J.D. (2010). Spectroscopic method for determination of the absorption coefficient in brain tissue. J. Biomed. Opt. *15*, 057005.

Kalmbach, A.S., and Waters, J. (2012). Brain surface temperature under a craniotomy. J. Neurophysiol. *108*, 3138–3146.

Kedenburg, S., Vieweg, M., Gissibl, T., and Giessen, H. (2012). Linear refractive index and absorption measurements of nonlinear optical liquids in the visible and near-infrared spectral region. Opt. Mater. Express *2*, 1588.

Kitamura, T., Ogawa, S.K., Roy, D.S., Okuyama, T., Morrissey, M.D., Smith, L.M., Redondo, R.L., and Tonegawa, S. (2017). Engrams and circuits crucial for systems consolidation of a memory. Science *356*, 73–78.

Kiyatkin, E.A. (2007). Brain temperature fluctuations during physiological and pathological conditions. Eur. J. Appl. Physiol. *101*, 3–17.

Klapoetke, N.C., Murata, Y., Kim, S.S., Pulver, S.R., Birdsey-Benson, A., Cho, Y.K., Morimoto, T.K., Chuong, A.S., Carpenter, E.J., Tian, Z., et al. (2014). Independent optical excitation of distinct neural populations. Nat. Methods *11*, 338–346.

Kobat, D., Durst, M.E., Nishimura, N., Wong, A.W., Schaffer, C.B., and Xu, C. (2009). Deep tissue multiphoton microscopy using longer wavelength excitation. Opt. Express *17*, 13354–13364.

Koester, H.J., Baur, D., Uhl, R., and Hell, S.W. (1999). Ca2+ fluorescence imaging with pico- and femtosecond two-photon excitation: signal and photodamage. Biophys. J. *77*, 2226–2236.

König, K., Becker, T.W., Fischer, P., Riemann, I., and Halbhuber, K.J. (1999). Pulse-length dependence of cellular response to intense near-infrared laser pulses in multiphoton microscopes. Opt. Lett. *24*, 113–115.

Kuhlman, S.J., and Huang, Z.J. (2008). High-resolution labeling and functional manipulation of specific neuron types in mouse brain by Cre-activated viral gene expression. PLoS ONE *3*, e2005.

Linz, N., Freidank, S., Liang, X.-X., and Vogel, A. (2016). Wavelength dependence of femtosecond laser-induced breakdown in water and implications for laser surgery. Phys. Rev. B *94*, 024113.

Lutz, C., Otis, T.S., DeSars, V., Charpak, S., DiGregorio, D.A., and Emiliani, V. (2008). Holographic photolysis of caged neurotransmitters. Nat. Methods *5*, 821–827.

Mortier, M., and Patriarche, G. (2000). Structural characterisation of transparent oxyfluoride glass-ceramics. J. Mater. Sci. *35*, 4849–4856.

Nagel, G., Brauner, M., Liewald, J.F., Adeishvili, N., Bamberg, E., and Gottschalk, A. (2005). Light activation of channelrhodopsin-2 in excitable cells of Caenorhabditis elegans triggers rapid behavioral responses. Curr. Biol. *15*, 2279–2284.

Noack, J., and Vogel, A. (1999). Laser-induced plasma formation in water at nanosecond to femtosecond time scales: calculation of thresholds, absorption coefficients, and energy density. IEEE J. Quant. Electron. *35*, 1156–1167.

Olivié, G., Giguère, D., Vidal, F., Ozaki, T., Kieffer, J.-C., Nada, O., and Brunette, I. (2008). Wavelength dependence of femtosecond laser ablation threshold of corneal stroma. Opt. Express *16*, 4121–4129.

Packer, A.M., Peterka, D.S., Hirtz, J.J., Prakash, R., Deisseroth, K., and Yuste, R. (2012). Two-photon optogenetics of dendritic spines and neural circuits. Nat. Methods *9*, 1202–1205.

Packer, A.M., Russell, L.E., Dalgleish, H.W.P., and Häusser, M. (2015). Simultaneous all-optical manipulation and recording of neural circuit activity with cellular resolution in vivo. Nat. Methods *12*, 140–146.

Papagiakoumou, E., de Sars, V., Oron, D., and Emiliani, V. (2008). Patterned two-photon illumination by spatiotemporal shaping of ultrashort pulses. Opt. Express *16*, 22039–22047.

Papagiakoumou, E., Anselmi, F., Bègue, A., de Sars, V., Glückstad, J., Isacoff, E.Y., and Emiliani, V. (2010). Scanless two-photon excitation of channelrhodopsin-2. Nat. Methods *7*, 848–854.

Papagiakoumou, E., Bègue, A., Leshem, B., Schwartz, O., Stell, B.M., Bradley, J., Oron, D., and Emiliani, V. (2013). Functional patterned multiphoton excitation deep inside scattering tissue. Nat. Photonics *7*, 274–278.

Pegard, N.M., Oldenburg, I., Sridharan, S., Walller, L., and Adesnik, H. (2017). Three-dimensional scanless holographic optogenetics with temporal focusing (3D-SHOT). Nat. Commun. *8*, 1228.

Pennes, H.H. (1948). Analysis of tissue and arterial blood temperatures in the resting human forearm. J. Appl. Physiol. *1*, 93–122.

Penzo, M.A., Robert, V., Tucciarone, J., De Bundel, D., Wang, M., Van Aelst, L., Darvas, M., Parada, L.F., Palmiter, R.D., He, M., et al. (2015). The paraventricular thalamus controls a central amygdala fear circuit. Nature *519*, 455–459.

Petreanu, L., Mao, T., Sternson, S.M., and Svoboda, K. (2009). The subcellular organization of neocortical excitatory connections. Nature *457*, 1142–1145.

Pisanello, F., Sileo, L., Oldenburg, I.A., Pisanello, M., Martiradonna, L., Assad, J.A., Sabatini, B.L., and De Vittorio, M. (2014). Multipoint-emitting optical fibers for spatially addressable in vivo optogenetics. Neuron *82*, 1245–1254.

Podgorski, K., and Ranganathan, G. (2016). Brain heating induced by near infrared lasers during multi-photon microscopy. bioRxiv *116*, 057364.

Pologruto, T.A., Sabatini, B.L., and Svoboda, K. (2003). ScanImage: Flexible software for operating laser scanning microscopes. Biomed. Eng. Online *2*, 1–9.

Prakash, R., Yizhar, O., Grewe, B., Ramakrishnan, C., Wang, N., Goshen, I., Packer, A.M., Peterka, D.S., Yuste, R., Schnitzer, M.J., and Deisseroth, K. (2012). Two-photon optogenetic toolbox for fast inhibition, excitation and bistable modulation. Nat. Methods *9*, 1171–1179.

Reig, R., Mattia, M., Compte, A., Belmonte, C., and Sanchez-Vives, M.V. (2010). Temperature modulation of slow and fast cortical rhythms. J. Neurophysiol. *103*, 1253–1261.

Rickgauer, J.P., and Tank, D.W. (2009). Two-photon excitation of channelrhodopsin-2 at saturation. Proc. Natl. Acad. Sci. U S A *106*, 15025–15030.

Rickgauer, J.P., Deisseroth, K., and Tank, D.W. (2014). Simultaneous cellular-resolution optical perturbation and imaging of place cell firing fields. Nat. Neurosci. *17*, 1816–1824.

Ronzitti, E., Conti, R., Zampini, V., Tanese, D., Foust, A.J., Klapoetke, N., Boyden, E.S., Papagiakoumou, E., and Emiliani, V. (2017). Sub-millisecond optogenetic control of neuronal firing with two-photon holographic photoactivation of Chronos. J. Neurosci. *37*, 10679–10689.

Saïdi, E., Samson, B., Aigouy, L., Volz, S., Löw, P., Bergaud, C., and Mortier, M. (2009). Scanning thermal imaging by near-field fluorescence spectroscopy. Nanotechnology *20*, 115703.

Schott, S., Bertolotti, J., Léger, J.-F., Bourdieu, L., and Gigan, S. (2015). Characterization of the angular memory effect of scattered light in biological tissues. Opt. Express *23*, 13505–13516.

Sharma, H.S., and Hoopes, P.J. (2003). Hyperthermia induced pathophysiology of the central nervous system. Int. J. Hyperthermia *19*, 325–354.

Shemesh, O.A., Tanese, D., Zampini, V., Linghu, C., Piatkevich, K., Ronzitti, E., Papagiakoumou, E., Boyden, E.S., and Emiliani, V. (2017). Temporally precise single-cell-resolution optogenetics. Nat. Neurosci. *20*, 1796–1806.

Shibasaki, K., Suzuki, M., Mizuno, A., and Tominaga, M. (2007). Effects of body temperature on neural activity in the hippocampus: regulation of resting membrane potentials by transient receptor potential vanilloid 4. J. Neurosci. *27*, 1566–1575.

Shin, Y., Yoo, M., Kim, H.-S., Nam, S.-K., Kim, H.-I., Lee, S.-K., Kim, S., and Kwon, H.-S. (2016). Characterization of fiber-optic light delivery and light-induced temperature changes in a rodent brain for precise optogenetic neuromodulation. Biomed. Opt. Express *7*, 4450–4471.

Stujenske, J.M., Spellman, T., and Gordon, J.A. (2015). Modeling the spatiotemporal dynamics of light and heat propagation for in vivo optogenetics. Cell Rep. *12*, 525–534.

Sun, B., Salter, P.S., Roider, C., Jesacher, A., Strauss, J., Heberle, J., Schmidt, M., and Booth, M.J. (2018). Four-dimensional light shaping: manipulating ultrafast spatiotemporal foci in space and time. Light Sci. Appl. *7*, 17117.

Szabo, V., Ventalon, C., De Sars, V., Bradley, J., and Emiliani, V. (2014). Spatially selective holographic photoactivation and functional fluorescence imaging in freely behaving mice with a fiberscope. Neuron *84*, 1157–1169.

Thompson, S.M., Masukawa, L.M., and Prince, D.A. (1985). Temperature dependence of intrinsic membrane properties and synaptic potentials in hippocampal CA1 neurons in vitro. J. Neurosci. *5*, 817–824.

Thomsen, S. (1991). Pathologic analysis of photothermal and photomechanical effects of laser-tissue interactions. Photochem. Photobiol. *53*, 825–835.

Vogel, A., Noack, J., Hüttman, G., and Paltauf, G. (2005). Mechanisms of femtosecond laser nanosurgery of cells and tissues. Appl. Phys. B Lasers Opt. *81*, 1015–1047.

Wang, H., Wang, B., Normoyle, K.P., Jackson, K., Spitler, K., Sharrock, M.F., Miller, C.M., Best, C., Llano, D., and Du, R. (2014). Brain temperature and its fundamental properties: a review for clinical neuroscientists. Front. Neurosci. *8*, 307.

Wang, Y., Deng, R., Xie, X., Huang, L., and Liu, X. (2016). Nonlinear spectral and lifetime management in upconversion nanoparticles by controlling energy distribution. Nanoscale *8*, 6666–6673.

Wells, J., Kao, C., Konrad, P., Milner, T., Kim, J., Mahadevan-Jansen, A., and Jansen, E.D. (2007). Biophysical mechanisms of transient optical stimulation of peripheral nerve. Biophys. J. *93*, 2567–2580.

Wu, Z., Autry, A.E., Bergan, J.F., Watabe-Uchida, M., and Dulac, C.G. (2014). Galanin neurons in the medial preoptic area govern parental behaviour. Nature *509*, 325–330.

Wyart, C., Del Bene, F., Warp, E., Scott, E.K., Trauner, D., Baier, H., and Isacoff, E.Y. (2009). Optogenetic dissection of a behavioural module in the vertebrate spinal cord. Nature *461*, 407–410.

Yang, W., Carrillo-reid, L., Bando, Y., Peterka, D.S., and Yuste, R. (2018). Simultaneous two-photon optogenetics and imaging of cortical circuits in three dimensions. eLife *7*, e32671.

Yaroslavsky, A.N., Schulze, P.C., Yaroslavsky, I.V., Schober, R., Ulrich, F., and Schwarzmaier, H.J. (2002). Optical properties of selected native and coagulated human brain tissues in vitro in the visible and near infrared spectral range. Phys. Med. Biol. *47*, 2059–2073.

Yizhar, O., Fenno, L.E., Davidson, T.J., Mogri, M., and Deisseroth, K. (2011). Optogenetics in neural systems. Neuron *71*, 9–34.

Zhang, Y.-P., and Oertner, T.G. (2007). Optical induction of synaptic plasticity using a light-sensitive channel. Nat. Methods *4*, 139–141.

STAR★METHODS

KEY RESOURCES TABLE

REAGENT or RESOURCE	SOURCE	IDENTIFIER
Bacterial and Virus Strains		
AAV2/8-hSyn-CoChR-GFP	Klapoetke et al., 2014	N/A
Experimental Models: Cell Lines		
Mouse for *in-vivo*: C57BL/6J	Janvier Labs	SC-C57J-M
Mouse for *in-vitro*: Swiss mice	Janvier Labs	RjOrl:SWISS
Software and Algorithms		
pCLAMP10	Molecular Devices	http://mdc.custhelp.com/
ScanImage 3	Pologruto et al., 2003	http://scanimage.org
Holographic and Scanning illumination thermal simulation (MATLAB)	This paper	Available as a Supplemental file
MATLAB R2017a	Mathworks inc., USA	http://mathworks.com
LabVIEW	National Instruments	http://www.ni.com/en-us.html
OriginPro 2016	OriginLab	https://www.originlab.com/Origin
AvaSoft8	Avantes	https://www.avantes.com
SlideBook 6	3i-Intelligent Imaging Innovations	https://www.intelligent-imaging.com/slidebook
Wavefront Designer 4	Photonics Department, Institut de la Vision, Paris	N/A

CONTACT FOR REAGENT AND RESOURCE SHARING

Further information and requests for resources and reagents should be directed to and will be fulfilled by the Lead Contact, Valentina Emiliani (valentina.emiliani@parisdescartes.fr).

EXPERIMENTAL MODEL AND SUBJECT DETAILS

Mice for *in vivo* experiments

All animal experiments were performed in accordance with the Directive 2010/63/EU of the European Parliament and of the Council of 22 September 2010. The protocols were approved by the Paris Descartes Ethics Committee for Animal Research with the registered number CEEA34.EV.118.12. Adult female or male C57BL/6J mice (Janvier Labs) were anesthetized with intraperitoneal injection of a ketamine-xylazine mixture (0.1 mg ketamine and 0.01 mg xylazine/g body weight) during stereotaxic injection and with isoflurane (2% for induction and 0.5%–1% for experiment) during photostimulation experiments. Cortical neurons of 4-week-old mice were transduced with viral vectors of opsins using stereotaxic injection. Photostimulation experiments were performed 5-8 weeks after injection.

Mice for in-vitro experiments

All experimental procedures were conducted in accordance with guidelines from the European Union and institutional guidelines on the care and use of laboratory animals (council directive 86/609 of the European Economic Community) that were approved by the Paris Descartes Ethics Committee for Animal Research (registration number CEEA34.EV.118.12). Stereotactic injections of the viral vectors AAV2/8-hSyn-CoChR-GFP (Shemesh et al., 2017) were performed in 4-week-old male Swiss mice (Janvier Labs). Animals were housed from 3 to 5 per cage with a light dark cycle of 12 + 12 h. Mice were anesthetized with a ketamine (80 mg/kg)-xylazine (5 mg/kg) solution and a small craniotomy (0.7 mm) was made on the skull overlying V1 cortex. An injection of 1–1.5 μl solution containing the viral vector was made with a cannula at about 80–100 nl/min at 200–250 μm below the dural surface. The skin was sutured, and the mouse recovered from anesthesia.

METHOD DETAILS

Virus injection and surgical procedures – In-vivo

Through a craniotomy over the right primary visual cortex (V1; 3.5 mm caudal from the bregma, 2.5 mm lateral from the midline), 1.5 μL viral vectors AAV2/8-hSyn-CoChR-GFP (Klapoetke et al., 2014; Shemesh et al., 2017) of were delivered via a cannula in

the layer 2/3 (250 μm deep) at a speed of 80-100 nL/min. For performing acute photostimulation *in vivo*, a circular craniotomy of 2 mm diameter was made over V1 and the dura mater was removed. Agarose of 0.5%–2% and a cover glass were applied on top of the craniotomy for stabilization/to dampen tissue movement.

2P-guided electrophysiology – in-vivo

Cortical neurons were targeted with patch pipettes under a custom-built 2P microscope equipped with a Ti:Sapphire laser (Chameleon Vision II, Coherent), and a 40x water-immersion objective (Nikon, CFI APO 40XW NIR, NA0.80). For a detailed description of the 2P scanning imaging system see (Chaigneau et al., 2016). The GFP labeling in opsin-expressing cells were visualized by excitation at 920 nm and the emitted fluorescence was collected through red (617/70 nm) and green (510/80 nm) filters (Semrock). Imaging data were acquired using ScanImage 3 software (http://scanimage.org).

Cell-attached recordings were obtained by using microelectrodes fabricated from borosilicate glass (5-8 M Ω resistance) and filled with solution containing the following (in mM): 135 potassium gluconate, 10 HEPES, 10 sodium phosphocreatine, 4 KCl, 4 Mg-ATP, 0.3 Na_3GTP, 25-50 Alexa Flour 594 for pipette visualization. The craniotomy was covered with the extracellular solution containing the following (in mM): 145 NaCl, 5.4 KCl, 10 HEPES, 1 $MgCl_2$, 1.8 $CaCl_2$. Voltage recordings in the current-clamp mode were acquired by using a MultiClamp 700B amplifier and a Digidata 1550A digitizer, which were controlled by a pCLAMP10 software (Molecular Devices). Electrophysiology data were filtered at 6 kHz and digitized at 20 kHz.

Holographic photostimulation – in-vivo

Holographic photostimulation was implemented with the imaging system mentioned above. Computer-generated holography was utilized for patterning light beams from an amplified fiber laser (Satsuma HP, Amplitude Systemes) at 1030 nm via a spatial light modulator (LCOS-SLM; X10468-07, Hamamatsu Photonics). The photostimulation setup was similar to the one described in (Ronzitti et al., 2017) and (Chaigneau et al., 2016). The SLM was controlled by a custom-designed software (Lutz et al., 2008). A cylindrical lens was introduced to suppress zero-order excitation (Hernandez et al., 2016).

2P photostimulation was performed using a circular holographic spot of 12-μm diameter covering the soma of a CoChR-positive neuron whose spiking activity was monitored through a patch pipette. A threshold power density between 0.05-0.5 $mW/\mu m^2$ of a 1-10 ms light pulse was determined for a target neuron to elicit an AP in 3-6 repetitions. A train of APs were elicited upon photostimulation with 5-10 illumination pulses at 10, 20 and 40 Hz.

Brain slices

Brain slices of V1 cortex were prepared from mice 7–15 weeks after viral injection. Mice were deeply anesthetized with isoflurane (5% in air) and decapitated, and the brain was rapidly removed. Sagittal slices 300 μm thick were obtained (VT1200S Leica Biosystems, Germany) in room temperature or ice-cold solution containing the following (in mM): 93 NMDG, 2.5 KCl, 1.25 NaH2PO4, 30 NAHCO3, 20 HEPES Acid, 25 Glucose, 2 thiourea, 5 Na-Ascorbate, 3 Na-Pyruvate, 0.5 CaCl2 and 10 MgCl2. Afterward, slices were transferred to a recovery chamber held at 35° for 45 min, in a bath containing the following (in mM): 125 NaCl, 2.5 KCl, 26 $NaHCO_3$, 1.25 NaH_2PO_4, 1 $MgCl_2$, 1.5 $CaCl_2$, 25 glucose, 0.5 ascorbic acid. All solutions were aerated with 95% O_2 and 5% CO_2 to a final pH of 7.4. Slices were placed in a recording chamber under the microscope objective and were patched while monitoring IR transmitted light images acquired at approximately video rate. Cells were patched at 40–70 μm depth and clamped at −70 mV in voltage-clamp configuration. Opsin expressing cells were identified via epifluorescence or 2P-scanning imaging.

Whole-cell recordings – in-vitro

Whole-cell patch clamp recordings were made using Multiclamp 700B amplifier and a Digidata 1440 digitizer and a PC running pClamp (Molecular Devices). Cell type was established based on morphology and AP firing properties. Membrane potential was kept at −70 mV with current injections ranging from −5 to −35 pA in current-clamp configuration. Voltage and current clamp recordings were filtered at 6–10 kHz and sampled at 20–50 kHz. Borosilicate glass pipettes (outer diameter 1.5 mm and inner diameter 0.86 mm) were pulled with a micropipette puller (Sutter Instruments) and filled with a solution containing the following (in mM): 130 potassium gluconate, 7 KCl, 4 Mg-ATP, 0.3 mM Na-GTP, 10 sodium phosphocreatine and 10 mM HEPES (pH adjusted to 7.28 with KOH; osmolarity 280 mOsm). Pipette resistance in the bath was 5–7 MΩ.

2P holographic and spiral scanning photostimulation – in-vitro

The optical system used is analogous to the one described above for the measure of the laser induced heating. In this experiment, the excitation laser (GOJI, Amplitude Systemes, here operated at a repetition rate of 2 MHz and laser pulse width of ∼300fs) could be alternatively directed onto two different optical paths, in order to generate either parallel holographic stimulation or spiral scanning stimulation. The former consisted in illuminating the whole cell body with a 15 μm diameter holographic spot (see description of the optical path in the Thermal measurement section). The latter consisted in the spiral scanning of the cell body with an almost diffraction limited spot (∼0.8 μm lateral size). The spiral trajectory was obtained by controlling the movement of the two galvomirrors using a SlideBook 6 commercial software (3i-Intelligent Imaging Innovations) and its parameters (7 tours, pitch 1 μm) were chosen to cover approximately the same surface of the holographic illumination. The two beams were focused on the sample by a 40x 0.8 NA water immersion Zeiss objective and the cell response to photostimulation was monitored by electrophysiological recording.

Modeling – Light source propagation and scattering

The spatial distribution of the source term, $\Gamma(\vec{r})$,can be calculated for the propagation of either a Gaussian or holographic light beam. To model the three-dimensional light scattering within an opaque tissue, we used a diffraction approach such as the angular spectrum of planes. Given a desired intensity distribution at the target plane we first used the Gerchberg-Saxton algorithm (Lutz et al., 2008) to calculate the electric field distribution $E_{SLM}(r,t) = A(x,y)e^{i\varphi(x,y)}$ at the SLM plane, where $\varphi(x,y)$ is the phase mask calculated by using the Gerchberg-Saxton based algorithm, and $A(x,y)$ is a Gaussian distribution reproducing the illumination beam at the SLM plane. The angular spectrum of plane waves (Goodman, 1996) is then used to propagate the $E_{SLM}(r,t)$ through the sample, step by step and adding a random phase to scramble the field after each step. The random phase mask is built up by using a set of scattering parameters, reproducing the scattering properties of brain tissue. These parameters have been calibrated and experimentally verified in (Bègue et al., 2013; Papagiakoumou et al., 2013), where we measured and modeled the effect of scattering on amplitude attenuation, spatial scale of speckle, and quality of focus after propagation of light through up to 550 μm of acute brain slices. These parameters reproduced the experimental scattering length at 800 nm for cortical brain (~135 μm). The same parameters at 1030 nm give an effective extinction coefficient (or characteristic length for the decrease of fluorescence as a function of depth) of 175 μm ± 13 μm (Figure S2 A).

This approach is only an approximation of actual light scattering, first because it accounts only for forward scattering (neglecting backscattering) and second because scattering occurs only at certain predetermined planes, after discrete steps, and not continuously while propagating in the tissue. Despite these limitations the approach has been used successfully *to model, for instance, the 2P fluorescence decay as a function* of depth (Bègue et al., 2013; Papagiakoumou et al., 2013) or the angular memory effect (Schott et al., 2015) in biological tissue.

Modeling – Time dependence of source term

Considering a laser pulse of average power P_{av} and duration τ, which is obtained from a train of fs pulses of peak power P_p and duration τ_p at a repetition rate *f*, $P_{av} = f\,\tau_p\,P_p$. The temporal dependence of the source term,$\Pi(t)$, can be expressed either as a continuous illumination pulse of average intensity P_a or as a train of *fs* pulses. The two approaches can be considered equivalent if the heat diffusion out of the region of interest (ROI; area over which the temperature is averaged, e.g., the cell surface or the Er-Yb co-doped glass particle surface) is negligible in the interval between two successive laser pulses $\Delta t = 1/f$. If this condition is verified, the temperature over the ROI remains quasi constant during Δt so that the energy of each successive laser pulse, $\tau_p\,P_p$ simply adds to the one of the others pulses. As a result the total energy during an illumination time, τ, will equalize that of a continuous pulse of energy $\tau\,P_{av}$, giving rise to the same temperature rise. If *a* is the lateral dimension of the area of interest this condition can be expressed in terms of the thermal diffusion length:

$$l_{th} = \sqrt{6D\Delta t} \ll a \rightarrow f \gg \frac{6D}{a^2} \tag{5}$$

For a temperature averaged over a 12 μm diameter spot this corresponds to $f \gg 23\ kHz$.

In the case of a low repetition rate fiber laser (500 kHz) the relative decay of temperature in a 6 μm or 1 μm radius circular area during the 2 μs between successive laser pulses is of the order of 0.01% and 0.3%, respectively. This relative decay is even more negligible in the case of a conventional mode-locked laser (80 MHz repetition rate, 12.5 ns between successive laser pulses). We therefore can consider that within this repetition rate range (500kHz - 80MHz), the time dependence of the source term can be well approximated by a continuous illumination pulse of average intensity, the difference in the temperature at a given time step being simply the difference between continuous integration and a rectangle rule numerical integration of the heat source (Figure S2 B).

We can also compare the expressions of the convolution of Green's function with $\Pi(t)$ for both cases. This can be done in *k*-space (or Fourier domain where the convolution with the source term is carried out as a multiplication), for the 1D Green's function:

$$\begin{aligned}\tilde{G}_1(k,\tau) &= \frac{1}{\tau}\int_0^{\tau} exp\Big(-D(2\pi k)^2 t\Big)dt \\ \tilde{G}_2(k,\tau) &= \frac{1}{N}\sum_0^{N-1} exp\Big(-D(2\pi k)^2 i\Delta t\Big)\end{aligned} \tag{6}$$

$\tilde{G}_1(k,\tau)$ and $\tilde{G}_2(k,\tau)$ are the expressions for respectively the average power continuous illumination pulse and the discrete sum of *N* successive laser pulses, where *k* is the spatial frequency. Carrying out the integration and the summation:

$$\begin{aligned}\tilde{G}_1(k,\tau) &= \frac{1-exp\Big(-D(2\pi k)^2 t\Big)}{D(2\pi k)^2\tau} \\ \tilde{G}_2(k,\tau) &= \frac{1}{N}\frac{1-exp\Big(-D(2\pi k)^2 N\Delta t\Big)}{1-exp\Big(-D(2\pi k)^2\Delta t\Big)}\end{aligned} \tag{7}$$

For $D(2\pi k)^2\Delta t \ll 1$ and noting that $N\Delta t = \tau$

$$\tilde{G}_2(k,\tau) \approx \frac{1}{N}\frac{1-exp\left(-D(2\pi k)^2 N\Delta t\right)}{1-\left(1-D(2\pi k)^2\Delta t\right)} = \frac{1-exp\left(-D(2\pi k)^2 N\Delta t\right)}{D(2\pi k)^2 N\Delta t} = \tilde{G}_1(k,\tau) \quad (8)$$

Modeling – Convolution with separable source term

For a continuous illumination pulse, $\Pi(t)$ can be written as $\Pi(t) = u(t) - u(t-\tau)$ where $u(t)$ is Heaviside's function and the convolution over time can be carried out the obtain a new Green's function

$$K(r,t) = G(r,t) * \Pi(t) = \frac{1}{4\pi Dr}\left[erfc\left(\frac{r}{2\sqrt{Dt}}\right)u(t) - erfc\left(\frac{r}{2\sqrt{D(t-\tau)}}\right)u(t-\tau)\right] \quad (9)$$

where $erfc(x)$ is the complementary error function. $K(r,t)$ must then be convoluted over space with $\Gamma(\vec{r})$ to obtain the spatiotemporal distribution of temperature:

$$T(r,t) = (K(r,t) * \Gamma(\vec{r}))\mu_a \quad (10)$$

Modeling – Moving laser spot

To model the case of a moving light source (e. g. for spiral or raster scanning illumination) we can take advantage of the linearity of the diffusion equation and of the convolution operator to write the source term as:

$$q(\vec{r},t) = \sum_i q_i\left(\vec{r} - \vec{r_i}, t - t_i\right) \quad (11)$$

The term representing the scanning source was expressed as a succession of square pulses, centered on $\vec{r_i}$ at time t_i and the total spatiotemporal heat distribution was obtained by summing the heat contribution of each individual spot. This approach is less computationally consuming than solving Equation (1) using a continuous illumination. To ensure that the discretization of the light source does not affect the spatiotemporal distribution of temperature we chose a spatial separation between the steps to be shorter than the thermal diffusion length. For example the illumination time, $t_{i+1} - t_i$, of 50 μs used for the spirals in Figure 4C corresponds to a diffusion length $l_{th} = \sqrt{6Dt} \approx 6.6\ \mu m$, which is much larger than the corresponding spatial step $\vec{r_{i+1}} - r_i = 0.3\ \mu m$.

Considering that the time to generate a temporally focused pattern (~ps) is much shorter than the heat diffusion time, the case of a temporally focused pattern (Figure 4B) has been treated as if the sample was continuously illuminated.

Modeling – The infinite media hypothesis

The infinite media hypothesis can be considered valid if the dimensions of the medium are large compared to the diffusion length. This condition is satisfied for the simulation of *in vivo* experiments at depth > 50 μm. For experiments *in vitro*, this condition is in general valid for the transversal dimension (x,y) but not for the axial direction. Briefly, considering that the experiments are carried out using water immersion objective and the fact that the thermal properties of water are sufficiently close to those of biological tissue, we can neglect the thermal interface above the sample and consider the condition for an infinite medium verified in this direction. On the contrary, we must consider the thermal interface between the sample and the glass coverslip by introducing boundary conditions to Equation (1) accounting for continuity of temperature and heat flux at this interface. Due to the mismatch in the properties between glass and tissue, the boundary conditions lead to a modified Green's function $G^*(\vec{r},t)$ which can be calculated numerically. After convolution of $G^*(\vec{r},t)$ and $q(\vec{r},t)$ we found that the infinite medium hypothesis leads to an overestimation of the temperature rise of the order of 15% for a holographic spot of 10 μm diameter focused 5 μm above the sample/glass interface.

For prolonged (seconds to minutes) scanning illumination, the boundary conditions start to play a key role giving rise to a maximum of the temperature rise at a plane different from the objective focal plane (Podgorski and Ranganathan, 2016), therefore under these conditions the infinite medium approximation is not valid.

Thermal measurement

Our goal is to validate our model by measuring the spatiotemporal temperature distribution at the cellular scale within a 3D isotropic medium that mimics the thermal properties of biological tissue. To do so we used Er-Yb co-doped glass particles (50% GeO2 – 40% PbO – 10% PbF2 – 1% ErF3 – 1% YbF3) which acts as a temperature probe due to its temperature-dependent luminescence, thanks to the optic properties of doped PbF2 crystallite (Aigouy et al., 2005; Dantelle et al., 2005; Mortier and Patriarche, 2000; Saïdi et al., 2009). After excitation by up-conversion with an infrared (980 nm) laser illumination, the ratio between the integrated intensity of two fluorescence lines around 525 and 550 nm varies with temperature (Aigouy et al., 2005; Saïdi et al., 2009), as shown in Figure S1B. This technique, which relies on an optical intensity ratio, provides a robust and absolute temperature measurement insensitive to optical excitation fluctuations.

This probe is inserted in the middle of a water/agar gel (mass fraction of agar: 0.005), at distances larger than the thermal diffusion length from the nearest interfaces and can therefore be considered embedded in a 3D isotropic measurement medium. The whole sample is surrounded laterally by two layers of silicone isolator (0.5 mm thick each, Invitrogen P24743) and sandwiched between two coverslips (No. 1, 140 μm thickness). Owing to the very low agar contents, the optical and thermal properties of this phantom are very close to those of water (and to the thermal properties of tissue). The small dimension of the thermal probe (much smaller and less thermally invasive than a conventional metal thermocouple) offers the possibility of measuring temperature at the cellular scale, which is compatible with the cellular spatial scale measurement we aim for. The detection scheme used to measure the fluorescence ratio has a sampling rate limited to 250 Hz and therefore we used illumination pulses longer than those used for the simulations (50 or 500 ms versus 3 ms) in order to have enough data points to fit the model function.

In order to obtain sufficient temperature sensitivity and a short (4ms) integration times, we used Er-Yb particles of roughly 10μm in diameter, therefore we could only measure the temperature rise averaged on a size comparable to the cell soma. Moreover, in order to avoid that the (unknown) absorption of the particle hampered the reliability of temperature measurement we placed the crystal at ∼30 μm from the location of the illumination spot. In this conditions the temporal evolutions for scanning and holography will look almost the same, and therefore we only performed the measurement under holographic light illumination. The measurements were performed on a system built around a commercial upright microscope (Zeiss, Axio Examiner Z1) coupled with two-pulsed infrared excitation path. The heat-inducing holographic excitation uses an amplified fiber laser (GOJI, Amplitude Systemes, λ = 1030 nm, operated at a repetition rate of 10 MHZ and laser pulse width of ∼250 fs). The laser beam is triggered by an acousto-optic modulator (MQ40-A2, AA Optoelectronic) and expanded to illuminate the screen of Spatial light modulator (LCOS-SLM X10468-07 Hamamatsu Photonics). The SLM plane was then projected by two telescopes (equivalent magnification of 0.5) on the back aperture of a 20x-1.0 NA water immersion Zeiss objective. To maximize output power, the back aperture was underfilled, resulting in the generation of a holographic beam of ∼0.5 effective NA. The SLM was addressed with phase profile calculated via Gerchberg-Saxton based algorithm, in order to generate a 15 μm diameter holographic circular spot over different positions of the sample. The zero and higher diffraction orders (> 1) were blocked before entering the microscope. The position dependent diffraction efficiency of the SLM (Hernandez et al., 2016) were compensated by adjusting the total laser power for each lateral displacement (Figure 1A) of the spot.

A second femtosecond laser source (Ti:Sapphire oscillator, laser pulse width ∼100 fs, repetition rate 80 MHz, tuned at 980 nm, Mai Tai DeepSee, Spectra-Physics) was used to excite the Er/Yb glass probe. The laser beam, modulated by a Pockel cells (350-80, Con-optics), entered a commercial 2P scanning head (VIVO 2-PHOTON, 3i-Intelligent Imaging Innovations), and was focused on the Er/Yb probe by adjusting the position of two galvanometric mirrors. The paths of the two infrared beams were coupled through a polarizer beam splitter. The position of the glass probe was identified through DIC imaging on a CMOS camera (Thorlabs DCC 1545M) and its fluorescence was collected by the confocal entrance of a fiber spectrometer (Avantes, ULS2048L-EVO).

Thermal measurement – Calibration of the probe

In Er/Yb codoped glasses, the $^2H_{11/2}$ and $^4S_{3/2}$ levels of Erbium are in thermal equilibrium, and their population, and thus the fluorescence ratio, are ruled by a Boltzmann law of the form:

$$\frac{I_{525}}{I_{550}} \propto \exp\left(\frac{-\Delta E}{kT}\right) = \mathrm{A}.\exp\left(-\frac{B}{T}\right) \tag{12}$$

where I_{525} and I_{550} are the integrated luminescence intensities at 525 nm and 550 nm, ΔE is the energy separation between the corresponding levels, k the Boltzmann constant, and T the temperature (in Kelvins). A and B are constant coefficients which need to be determined by calibration, since they strongly depend on the nature and environment of the glass. Once A and B are known, the absolute temperature can be deduced quantitatively from measurements of I_{525}/I_{550} (Aigouy et al., 2005; Saïdi et al., 2009).

To do the calibration, the sample was heated on a PID-controlled heating element (Thorlabs, HT10K). A thin thermocouple (Omega, HYP0-33-1-T-G-60-SMP-M) implemented in the sample measured the temperature of the medium. At the same time, the probe was illuminated, and its luminescence spectrum was measured to derive $I_{525}/I_{550,}$ as a function of T. These measurements were achieved at thermal equilibrium, between 296.6 K and 309.8 K, and repeated to increase the reliability of the calibration. A linear fit on $\ln(I_{525}/I_{550})$ as a function of 1/T, shown in Figure S1 B, yielded the values of A and B with a coefficient of determination $R^2 = 0.9362$ (Figure S1 B).

QUANTIFICATION AND STATISTICAL ANALYSIS

In each experiment of Figure 4, multiple mice (n = 3 or n = 4) were analyzed as biological replicates. When we refer to the mean temperature rise, we perform the sum of the temperature rise in each pixel inside the spot of interest, and then divide by the number of pixels considered.

DATA AND SOFTWARE AVAILABILITY

The model has been implemented in a MATLAB (MathWorks) package that can be found as a supplemental zip file (see Data S1). Two main folders are in the archive, the first one with a master script and a library of functions for Holography simulations, and the second one following the same organization, but for Scanning simulations.